ACS APPLIED MATERIALS & INTERFACES

Research Article

www.acsami.org

Polymorphic $CoSe_2$ with Mixed Orthorhombic and Cubic Phases for Highly Efficient Hydrogen Evolution Reaction

Hongxiu Zhang, Bin Yang, Xiaolin Wu, Zhongjian Li, Lecheng Lei, and Xingwang Zhang*

Key Laboratory of Biomass Chemical Engineering of Ministry of Education, College of Chemical and Biological Engineering, Zhejiang University, Hangzhou, Zhejiang Province 310027, China

Supporting Information

ABSTRACT: We report polymorphic $CoSe_2$ (p-$CoSe_2$) with mixed orthorhombic and cubic phases as a highly active electrocatalyst toward hydrogen evolution reaction (HER). The p-$CoSe_2$ is obtained by calcining $CoSe_x$ via electrodeposition at 300 °C. The results of X-ray diffraction (XRD) and high-resolution transmission electron microscopy (HRTEM) demonstrated the crystal structure of p-$CoSe_2$. The p-$CoSe_2$ exhibits excellent electrocatalytic activity for HER with a low onset overpotential of −70 mV and a small Tafel slope of ∼30 mV/decade, which are basically state-of-the-art performance of earth-abundant electrocatalysts. The HER performance of p-$CoSe_2$ was much higher than that of amorphous $CoSe_x$, cubic $CoSe_2$, and CoSe. This study offers a competitive electrocatalyst for HER and opens up a new strategy to the synthesis of catalysts for energy conversion.

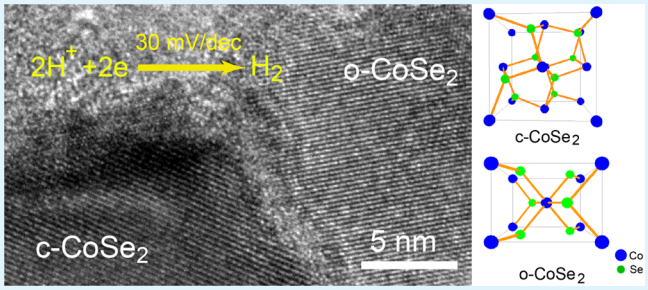

KEYWORDS: *polymorphic $CoSe_2$, hydrogen evolution reaction, electrodeposition, earth-abundant elements, electrocatalysis*

INTRODUCTION

Water splitting is a low-cost and environmentally friendly method for obtaining hydrogen energy, which is clean and sustainable. However, electrolysis of H_2O consumes large amounts of energy. In order to increase the efficiency of electrolysis, it is necessary to develop highly active electrocatalysts toward hydrogen evolution reaction (HER), which is commonly the key step in H_2O splitting.[1,2] Pt-based materials are highly efficient HER electrocatalysts, but the scarcity and high cost has prevented their application at large scale.[3] Therefore, perusing highly active HER catalysts, which are comprised of cheap and earth-abundant elements, is urgent and necessary.[4]

In the past decade, tremendous efforts have been made to develop efficient HER electrocatalysts based on non-noble and earth-abundant elements including metals, metal compounds, and nonmetals (carbon based).[5−11] Nickel and its alloys are commercial HER electrocatalysts, but they are not stable in acidic solution.[4,12] Many metal compounds such as transition metal dichalcogenides (MX_2) including MoS_2,[13] WS_2,[14] $MoSe_2$,[15] CoS_2,[16] $CoSe_2$,[17−19] etc., metal carbides (Mo_2C,[9,20] WC[21]), metal boride (MoB),[22] metal nitrides ($NiMN_x$),[23] and metal phosphides (Ni_2P,[24] CoP,[25,26] MoP,[27] and FeP[28]) have been identified as promising HER catalysts. Generally, most of them exhibited low intrinsic activity toward HER as compared with Pt. Consequently, various strategies have been investigated to improve the HER performance of electrocatalysts: (1) fabrication of nanostructured electrocatalysts with highly active surface areas;[28−32] (2) supporting catalysts onto conductive supports such as graphene;[33−35] (3) chemically exfoliating and simultaneously converting the semiconducting phases to their metallic phases (MoS_2,[36] WS_2[37]); (4) synthesis of amorphous polymorphs containing a high density of catalytic sites;[38] (5) alloying or doping catalysts to increase active sites.[39,40] So far, these approaches have greatly improved the HER performances of catalysts, but most of them still have no match for Pt; therefore, it is still highly desirable and imperative to fabricate electrocatalysts with the activity comparable to Pt.

In this study, we report a HER electrocatalyst, i.e., polymorphic $CoSe_2$ (p-$CoSe_2$, a typical MX_2) with mixed orthorhombic and cubic phases by calcining amorphous $CoSe_x$ fabricated by the electrodeposition method. The p-$CoSe_2$ exhibits a much higher HER performance, with a Tafel slope of ∼30 mV/decade (similar to Pt), as compared with amorphous $CoSe_x$ (∼40 mV/decade),[41,42] cubic $CoSe_2$ (∼40 mV/decade),[17−19] and CoSe (∼55 mV/decade). Structural characterizations using X-ray diffractometer, high resolution transmission electron microscopy, and X-ray photoelectron spectroscopy confirmed the crystal structure of p-$CoSe_2$. This work not only presents p-$CoSe_2$ as a cheap and highly active electrocatalyst with an excellent stability toward HER but also provides an effective strategy for improving the performance of earth-abundant electrocatalysts in general.

Received: October 23, 2014
Accepted: January 6, 2015
Published: January 6, 2015

DOI: 10.1021/am507373g
ACS Appl. Mater. Interfaces 2015, 7, 1772−1779

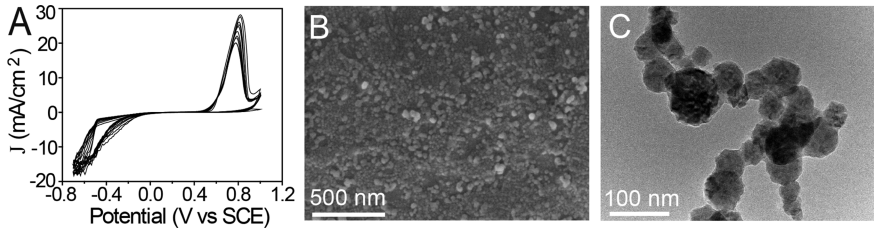

Figure 1. (A) Cyclic voltammograms recorded on a GD electrode during the $CoSe_x$ electrodeposition. The potential scan rate is 20 mV/s. (B) A typical SEM image of as-synthesized $CoSe_x$ calcined at 300 °C. (C) A TEM image of $CoSe_x$ nanoparticles calcined at 300 °C.

EXPERIMENTAL SECTION

Synthesis of $CoSe_x$ Supported on Graphite Disk (GD). The preparation of amorphous $CoSe_x$ films on GD was carried out using electrodeposition. The electrolyte solution was prepared by mixing 1 equiv of cobalt(II) chloride and 1 equiv of selenium dioxide (see the Supporting Information). Cyclic voltammograms (scan rate, 20 mV/s) recorded an oxidation peak at E_{pa} = 0.75 V vs Hg/Hg_2Cl_2, as shown in Figure 1A, and the reduction peak was not significant due to the multistep reactions. The electrodeposition of amorphous $CoSe_x$ films was performed at −0.7 V vs Hg/Hg_2Cl_2 for 40 min (see the experimental details in the Supporting Information). First, the precursor of SeO_2 is hydrolyzed to H_2SeO_3, which will be further reduced to selenium. Subsequently, most of the selenium will be reduced to Se_x^{2-}. The Co^{2+} from the electrolyte will move to the electrode surface, where the Se_x^{2-} bonds with Co^{2+} to form amorphous $CoSe_x$ films. We tentatively proposed that the deposition process was achieved through the following four steps (eqs 1−4):[41−43]

$$SeO_2 + H_2O \rightarrow H_2SeO_3 \quad (1)$$

$$H_2SeO_3 + 4H^+ + 4e^- \rightarrow Se(s) + 3H_2O \quad (2)$$

$$Se(s) + xe^- \rightarrow Se_x^{2-} \quad (3)$$

$$Se_x^{2-} + Co^{2+} \rightarrow CoSe_x(s) \quad (4)$$

Then, the as-synthesized $CoSe_x$/GD samples were dried under a vacuum at 40 °C, followed by calcination at different temperatures (250, 300, 450, and 600 °C) under argon for 40 min in a homemade tube reactor.

Electrochemical Measurements. The electrocatalytic activity of samples for HER was studied in 0.5 M H_2SO_4 solution purged with H_2 (99.999%) and recorded on a Bio-Logic SP 300 Potentiostat at ambient temperature. All tests were performed in a three-electrode electrochemical cell with a saturated Hg/Hg_2Cl_2 reference electrode and a graphite rod counter electrode. $CoSe_x$/GD, p-$CoSe_2$/GD, c-$CoSe_2$/GD, and CoSe/GD were used as the working electrodes to investigate their electrocatalytic activities toward HER. The reversible hydrogen electrode (RHE) was calibrated using a platinum wire as the working electrode to +0.260 V vs SCE, and H_2 was purged during the reaction.

Characterization. Scanning electron microscopy (SEM) was performed on a SIRON-100 (FEI America) field emission scanning electron microscope coupled with energy dispersive X-ray (EDX) spectra. The samples were pretreated by spraying gold for 30 s before the observation. The crystal structures of samples were characterized by an X'Pert PRO X-ray diffractometer (XRD) (PNAlytical Netherlands) using Cu Kα radiation (λ = 1.54056 Å), employing a sampling width of 0.033° in the 2θ range 10−90°. X-ray photoelectron spectroscopy (XPS) was performed using a VG ESCALAB MARK II XPS system with an Al Kα source. Binding energies were calibrated to the adventitious C 1s peak at 284.6 eV. The high-resolution transmission electron microscopy (HRTEM) images were gained by a field emission transmission electron microscope (TecnaiG2 F20 S-TWIN America) at an accelerating voltage of 200 kV.

RESULTS AND DISCUSSION

Catalyst Structure and Composition. The morphology of the as-prepared $CoSe_x$ calcined at different temperatures (250, 300, 450, and 600 °C) grown on the graphite disk (GD) was investigated with SEM. It was found that the as-synthesized $CoSe_x$ films calcined at 300 °C (Figure 1B) consisted of nanoparticles ranging from 50 to 100 nm in diameter, and most of them were about 50 nm in diameter, which was also confirmed by the TEM image, as shown in Figure 1C. The as-synthesized $CoSe_x$ calcined at 450 °C (Figure S1C, Supporting Information) and 600 °C (Figure S1D, Supporting Information) showed a similar morphology (films consisted of nanoparticles) with $CoSe_x$ calcined at 300 °C. Moreover, it was found that the particles in $CoSe_x$ calcinated at 450 °C were about 70 nm in diameter (Figure S2A, Supporting Information), while the particle size of 600 °C samples became larger, with a size of about 100 nm in diameter (Figure S2B, Supporting Information). The increase in the particle size of $CoSe_x$ caused by the calcination temperature was attributed to the growth and agglomeration of crystal particles. It was noteworthy that $CoSe_x$ calcined at 250 °C was mainly composed of amorphous $CoSe_x$ films and a small amount of crystal particles, as shown in Figure S1A and B (Supporting Information). The molar Se/Co ratio of the $CoSe_x$ films was about 2.22, as shown in Figure S1F (Supporting Information). The particle size of the crystal particles was about 1−2 μm, which possibly resulted from the crystallization of amorphous $CoSe_x$. The crystal particles existed as cubic $CoSe_2$ confirmed by XRD analysis, as shown in Figure 2.

The crystal structures of the as-prepared $CoSe_x$ products calcined at different temperatures are revealed by XRD, as shown in Figure 2. For the 250 °C sample, the XRD pattern showed very weak diffraction peaks at 31.1 and 51.7° indexed to the planes of cubic $CoSe_2$ (defined as c-$CoSe_2$),[42] suggesting the amorphous $CoSe_x$ and tiny amounts of c-$CoSe_2$. Notably, when the calcination temperature was 300 °C, the $CoSe_x$ converted to polymorphic $CoSe_2$ (defined as p-$CoSe_2$) with mixed orthorhombic $CoSe_2$ (defined as o-$CoSe_2$) (PDF 10-0408, Pmnn (58), a = 3.6, b = 4.84, c = 5.72) and c-$CoSe_2$ (PDF 88-1712, Pa-3(205), $a = b = c$ = 5.8593).[44,45] The peaks at 30.81, 34.74, and 36.34° were attributed to characteristic peaks of the o-$CoSe_2$, and the peaks at 43.6 and 51.7° were assigned to c-$CoSe_2$.When the calcination temperature was further increased to 450 °C, the product was pure c-$CoSe_2$ confirmed by the XRD pattern (PDF 88-1712), where the peaks at 34.2, 37.7, 51.9, and 58.9° were indexed to (210), (211), (311), and (321) of c-$CoSe_2$. It was concluded that the crystal structure of $CoSe_2$ converted from an orthorhombic space group to a cubic space group when the calcination temperature rose from 300 to 450 °C. When the calcination temperature increased to 600 °C, CoSe (PDF 89-2004, P6-

DOI: 10.1021/am507373g
ACS Appl. Mater. Interfaces 2015, 7, 1772−1779

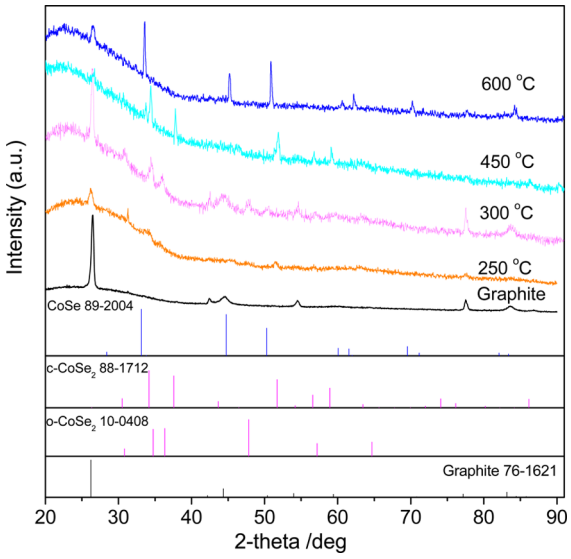

Figure 2. XRD patterns of the as-prepared $CoSe_x$/GD samples calcined at different temperatures.

3mc, $a = b = 3.6294$, $c = 5.3006$) with peaks at 33.41, 45.01, and 50.81° was observed, suggesting a conversion from c-$CoSe_2$ to CoSe during calcination.[46,47]

The crystal structures of $CoSe_x$ calcined at different temperatures were further confirmed with HRTEM, as shown in Figure 3. In the case of p-$CoSe_2$ (300 °C), as shown in Figure 3A, the HRTEM image exhibited clear crystal lattices belonging to o-$CoSe_2$ and c-$CoSe_2$. The resolved lattice fringes of o-$CoSe_2$ (012) plans with a spacing of 2.47 Å and c-$CoSe_2$ (200) plans with a spacing of 2.93 Å were clearly revealed. Moreover, the corresponding fast Fourier transform (FFT) images further revealed the existence of mixed o-$CoSe_2$ and c-$CoSe_2$, as shown in Figure 3A (right). The crystal structure of c-$CoSe_2$ (450 °C) was confirmed using the resolved lattice fringes of c-$CoSe_2$ (200) plans with a spacing of 2.93 Å, c-$CoSe_2$ (210) plans with a spacing of 2.62 Å, and c-$CoSe_2$ (211) plans with a spacing of 2.39 Å, as shown in Figure 3B. The crystal structure of CoSe (600 °C) was also confirmed by CoSe (110) plans with a spacing of 1.81 Å, as presented in Figure 3C. These results are consistent with the XRD analysis of $CoSe_x$ calcined at different temperatures, as illustrated in Figure 2.

The valence and chemical composition of samples were gained through XPS measurements, as shown in Figure 4. In the p-$CoSe_2$ (300 °C) sample, as shown in Figure 4A, the Co $2p_{3/2}$ signal can be fitted into two chemical states at binding energies of 778.5 and 781.1 eV. The dominant peak (41%) in the Co $2p_{3/2}$ XPS spectrum at 778.5 eV indicates the presence of Co−Co, and the relatively weak peak (25.2%) at 781.1 eV is from Co^{2+} coordinated to Se ions.[27,48,49] The peak at 793.5 eV is assigned to Co $2p_{1/2}$.[50] The Se $3d_{5/2}$ signal of p-$CoSe_2$ (300 °C) can be fitted into two chemical states at binding energies of 54.8 and 56.3 eV, as shown in Figure 4B. The major peak at 54.8 eV is attributed to the Co−Se bond.[51] The peaks at 56.3 and 59.2 eV correspond to Se $3d_{5/2}$ (Se−Se) and Se $3d_{3/2}$,[49] respectively. In the case of CoSe (600 °C), as presented in Figure 4C, the Co $2p_{3/2}$ signal can be fitted into four chemical states, which are ascribed to some intermediate valence generated in the conversion process from c-$CoSe_2$ to CoSe. It can be observed that one characteristic peak at 778.7 eV is attributed to the Co $2p_{3/2}$ binding energies for a Co (II)

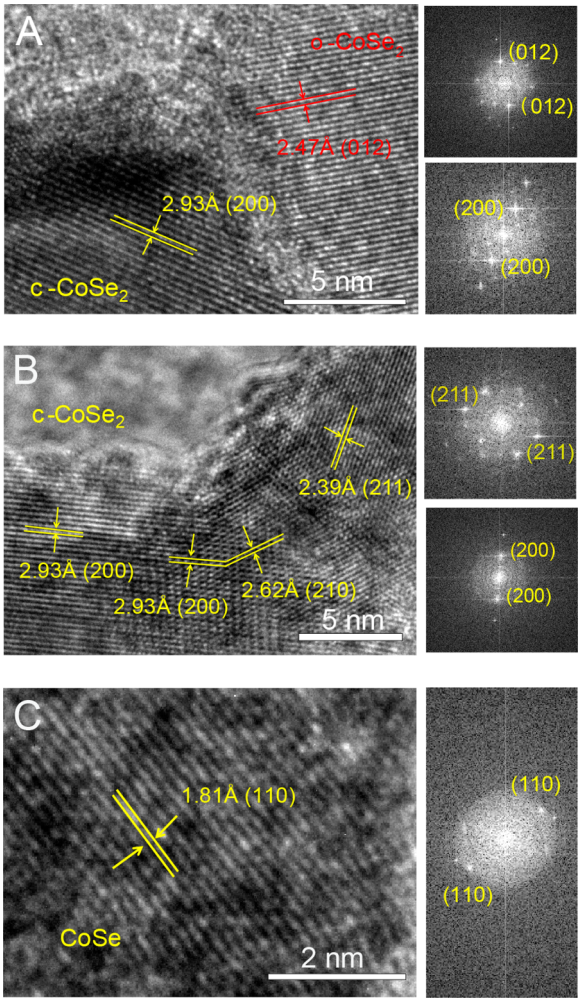

Figure 3. HRTEM images and the corresponding fast Fourier transform (FFT) images of p-$CoSe_2$ calcined at 300 °C (A), c-$CoSe_2$ calcined at 450 °C (B), and CoSe calcined at 600 °C (C).

oxidation state, indicating the existence of CoSe.[47,52] The Se $3d_{5/2}$ (54.8 eV) and Se $3d_{3/2}$ (59.2 eV) were also observed in the XPS spectra of CoSe (600 °C), as shown in Figure 4D. It was noteworthy that Se $3d_{5/2}$(Se−Se) at 56.3 eV disappeared, suggesting the chemical state change of Se. The XPS spectra of $CoSe_x$ calcined at 250 and 450 °C were illustrated in Figures S3A/B and C/D (Supporting Information), respectively. These two samples exhibited similar XPS characteristics as compared with p-$CoSe_2$ (300 °C), which are obviously attributed to their similar chemical compositions.

On the basis of the above structural characterizations, it seemed that $CoSe_x$ conversion to $CoSe_2$ and decomposition of $CoSe_2$ proceeded through the following possible reactions:

$$CoSe_x(s) \rightarrow \text{o-}CoSe_2(s) + \text{c-}CoSe_2(s) + Se(g), \quad 300\ ^\circ C \tag{5}$$

$$\text{o-}CoSe_2(s) \rightarrow \text{c-}CoSe_2(s), \quad 450\ ^\circ C \tag{6}$$

$$\text{o-}CoSe_2(s) \rightarrow CoSe + Se(g), \quad 600\ ^\circ C \tag{7}$$

When $CoSe_x$ is calcined at 300 °C, the crystallization will occur and results in the formation of $CoSe_2$, and the excessive Se in $CoSe_x$ (the molar Se/Co ratio >2), as shown in Figure S1E and F (Supporting Information), would be released (eq 5).

DOI: 10.1021/am507373g
ACS Appl. Mater. Interfaces 2015, 7, 1772−1779

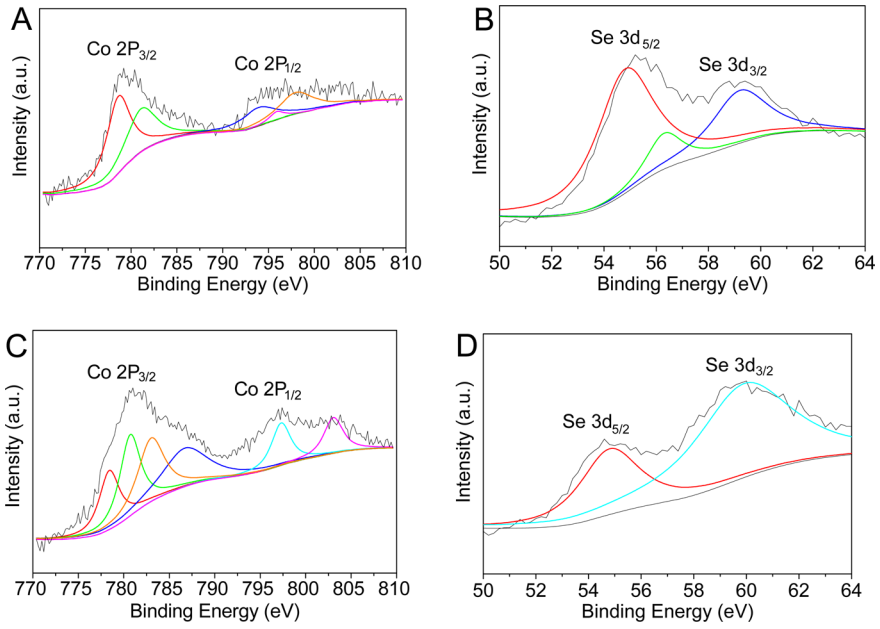

Figure 4. XPS of the Co 2p and Se 3d regions for p-$CoSe_2$ calcined at 300 °C (A, B) and CoSe calcined at 600 °C (C, D).

Since the o-$CoSe_2$ and c-$CoSe_2$ phases have the similarity structure and the small lattice mismatch resulting in the easy epitaxial growth between them,[18,53] polymorphic $CoSe_2$ (p-$CoSe_2$) with mixed orthorhombic and cubic phases is produced. When the calcination temperature is 450 °C, o-$CoSe_2$ is transformed to c-$CoSe_2$ (eq 6) because of the low activation energy of the interfacial nucleation process of the formation of c-$CoSe_2$.[54−56] A higher calcination temperature of 600 °C results in the decomposition of c-$CoSe_2$ to CoSe (eq 7), which is reported to be a thermodynamic favor process.[57]

HER Activities of Catalysts. The electrocatalytic HER activities of amorphous $CoSe_x$ (250 °C), p-$CoSe_2$ (300 °C), c-$CoSe_2$ (450 °C), and CoSe (600 °C), with the same electrodeposition time (40 min) of $CoSe_x$, were investigated in 0.5 M H_2SO_4 solution using a three-electrode setup (see the Supporting Information for experimental details). Polarization curves after *i*R corrected (see the Supporting Information for correction details) showing the geometric current density (J) plotted against the applied potential of various samples are exhibited in Figure 5A and B. It was interestingly seen that all samples exhibited high current densities ($J_{cathodic}$ > 100 mA cm^{-2}) under very low applied overpotentials; moreover, the calcination temperature had a strong influence on the current densities of samples. Notably, p-$CoSe_2$ (300 °C) showed an onset of HER activity at about −70 mV (vs RHE) and significant H_2 evolution ($J_{cathodic}$ = 10 mA cm^{-2}) at approximately −0.15 V (vs. RHE). In contrast, the cathodic overpotentials for significant H_2 evolution ($J_{cathodic}$ = 10 mA cm^{-2}) of $CoSe_x$ (250 °C), c-$CoSe_2$ (450 °C), and CoSe (600 °C) were 0.18, 0.20, and 0.27 V, respectively. The onset potentials and the cathodic overpotentials for significant H_2 evolution ($J_{cathodic}$ = 10 mA cm^{-2}) of samples calcined at different temperatures are summarized in Table S1 (Supporting Information). It was seen that p-$CoSe_2$ (300 °C) exhibited the highest overall HER performance, as shown in Table S1 (Supporting Information). The significant differences in HER activities of different samples resulted from the significant differences in the intrinsic activities, which were revealed by comparing the Tafel slopes (Figure 5C) of p-$CoSe_2$ (31.2 mV/decade), $CoSe_x$ (38.3 mV/decade), c-$CoSe_2$ (38.8 mV/decade), and CoSe (55.4 mV/decade). We also measured the double layer capacitances (C_{dl}) of samples calcined at different temperatures, because it is considered to be a parameter affecting the HER performance of samples. It was found that C_{dl} values of $CoSe_x$ (250 °C), p-$CoSe_2$ (300 °C), c-$CoSe_2$ (450 °C), and CoSe (600 °C) were 24.7, 20.4, 11.8, and 9.1 mF/cm^2, as shown in Figure S5 (Supporting Information). C_{dl} is commonly thought to be proportional to the effective electrochemically active surface area of the electrode−electrolyte interface of electron transfer in HER, and it is mainly determined by the surface area of the electrode, surface properties such as hydrophilicity/hydrophobicity, and electrocatalytic activity (per-site turnover frequency) of samples. In this study, samples calcined at different temperatures are films, and the particle sizes of these samples did not change too much, as shown in Figure 1C and Figure S2 (Supporting Information), so the particle size would not have a strong influence on the surface area of the samples. In contrast, the intrinsic activities of samples (the Tafel slopes) were significantly different, as shown in Figure 5C. The differences in C_{dl} values were not mainly caused by the different particle sizes of samples calcined at different temperatures. Therefore, the differences of particle sizes would not play the key role in the HER performances of these samples.

Of note, the intrinsic activity of p-$CoSe_2$ (a Tafel of 31.2 mV/decade) is close to Pt (a Tafel of 30 mV/decade[36]) and much lower than that of c-$CoSe_2$ (a Tafel of ∼40 mV/decade).[18,19] The HER performance of p-$CoSe_2$ compares favorably with metal phosphides (Ni_2P,[24] CoP,[25,26] MoP,[27] and FeP[28]), synthesized by the complicated processes or with the use of the special organic precursors, which have state-of-the-art value of HER performance of the low onset overpotential (∼70 mV) and the high intrinsic activity (a Tafel of ∼30 mV/decade).

To explore the charge-transfer mechanism of HER on samples calcined at different temperatures, electrochemical impedance spectroscopy (EIS) ranging from 200 kHz to 50 mHz was used to investigate the reaction kinetics on the

DOI: 10.1021/am507373g
ACS Appl. Mater. Interfaces 2015, 7, 1772−1779

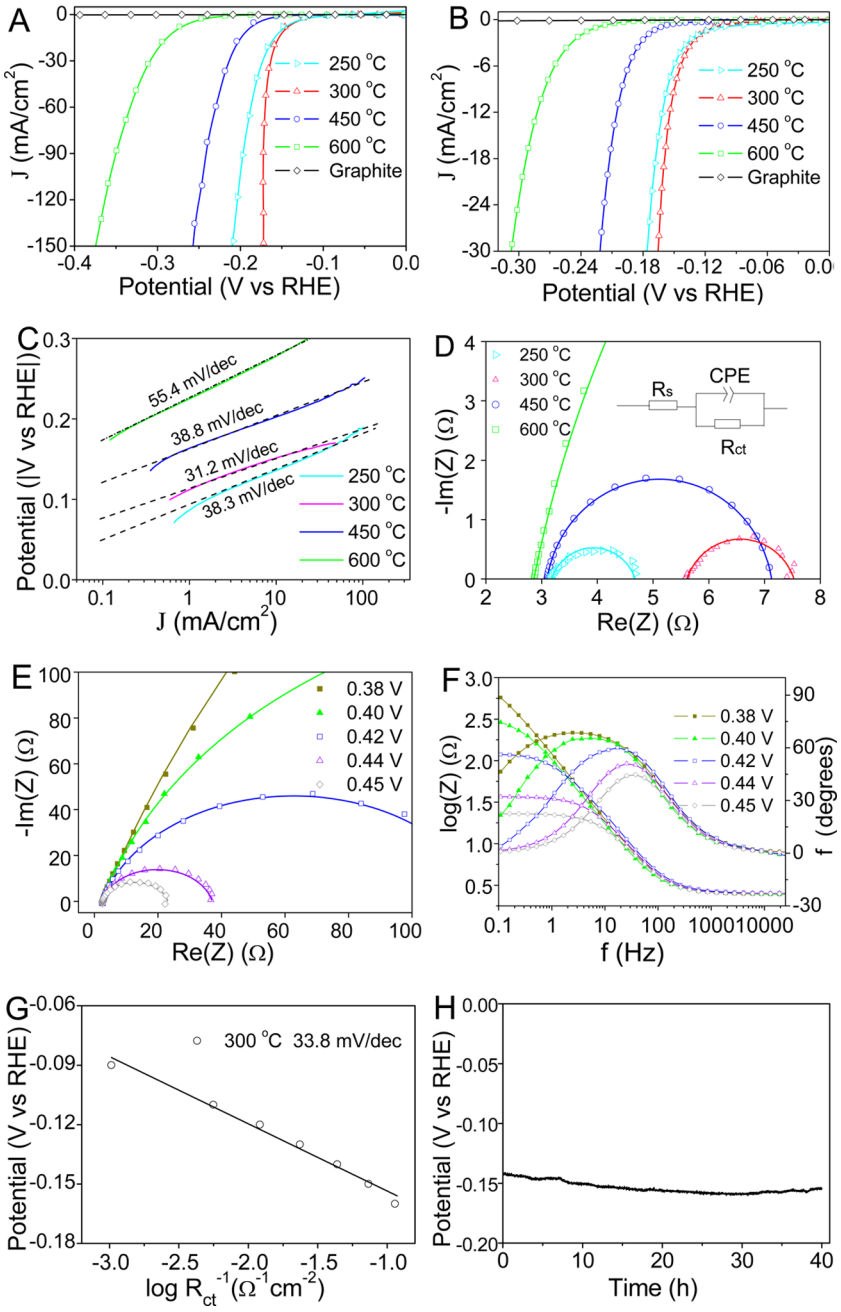

Figure 5. Polarization curves at (A) higher and (B) lower applied overpotentials of $CoSe_x$ (250 °C), p-$CoSe_2$ (300 °C), c-$CoSe_2$ (450 °C), and CoSe (600 °C). (C) Tafel slopes derived from *I*−*V* curves in part A. (D) Nyquist plots for the HER carried out under an overpotential of −0.5 V (vs SCE). The data was fitted with the simplified Randles equivalent circuit (inset), and the fitting results were shown as solid traces. (E) Nyquist plots carried out under different overpotentials (vs SCE) of p-$CoSe_2$. (F) Bode curves corresponding to the Nyquist curves of part E. (G) Semilogarithmic plot of the inverse charge-transfer resistance (R_{ct}^{-1}) as a function of overpotentials. (H) Long-term stability measurement for a representative of p-$CoSe_2$ (300 °C) suggesting the small change in the applied overpotential required to maintain a continuous electrocatalytic current density of −10 mA/cm^2 for 40 h. The electrodeposition time of all samples is 40 min.

electrode and to explore the different electrode/electrolyte interfaces on various samples under the same operating conditions.[58,59] Figure 5D shows the Nyquist plots for amorphous $CoSe_x$ (250 °C), p-$CoSe_2$ (300 °C), c-$CoSe_2$ (450 °C), and CoSe (600 °C). We further investigate the difference of the charge resistance (R_{ct}), which is associated with the reaction activity toward H_2(g) evolution (Figure 5D, inset), as shown in Table S1 (Supporting Information).[60] The R_{ct} values were the following: amorphous $CoSe_x$ (1.8 Ω), *p*-$CoSe_2$ (2.0 Ω), c-$CoSe_2$ (4.1 Ω), and CoSe (88.7 Ω). These R_{ct} values basically followed the trend of increasing Tafel slopes of the corresponding samples, suggesting the superior activities of samples might be attributed to the more facile kinetics toward H_2(g) evolution (the lower Tafel slopes).

We further use EIS to calculate the Tafel slope of the proton discharging step of HER on p-$CoSe_2$.[20,59,60] The Nyquist and Bode plots of the EIS response conducted at different overpotentials of p-$CoSe_2$ (300 °C) are shown in parts E and F of Figure 5, respectively. It was seen that all spectra consisted of a single semicircle, indicating the corresponding equivalent

DOI: 10.1021/am507373g
ACS Appl. Mater. Interfaces 2015, 7, 1772−1779

circuit (the simplified Randles equivalent circuit) for the HER kinetics could be characterized by one time constant.[61] Investigations into the dependence of the obtained impedances with overpotentials demonstrated that the gradient of log-(R_{ct}^{-1}) versus overpotential corresponded to the Tafel slope of the proton discharging step.[20] The overpotential is plotted versus the inverse R_{ct} on a logarithmic scale, as shown in Figure 5G. A good linear variation was observed for log(R_{ct}^{-1}) versus overpotential with a slope of 33.8 mV/decade obtained from the linear dependence (Figure 5G), which was quite close to the Tafel slope of 31.2 mV/decade derived from the linear sweep voltammograms, as shown in Figure 5C.

As we know, there are three possible main reaction steps for the HER in acidic solutions, which are commonly named the Volmer, Heyrovsky, and Tafel reactions, respectively:[20,30,62]

Volmer reaction:

$$H_3O^+ + e^- \rightarrow H_{ads} + H_2O \quad (8)$$

Heyrovsky:

$$H_{ads} + H_3O^+ + e^- \rightarrow H_2 + H_2O \quad (9)$$

Tafel:

$$H_{ads} + H_{ads} \rightarrow H_2 \quad (10)$$

According to previous reports, a slope of ~120 mV/decade indicates that the Volmer reaction is the rate-determining step of the HER. When the Heyrovsky or Tafel reactions are the rate-limiting steps, Tafel slopes would be ~40 and ~30 mV/decade, respectively. The Tafel slope is commonly an inherent characteristic of the electrocatalyst. For the p-$CoSe_2$ electrode, the Tafel slope of 31.2 mV/decade (Figure 5C) suggests that the Tafel reaction is the rate-limiting step of HER. Such a small Tafel slope in this study is expected to be beneficial for practical HER applications such as photoelectrochemical hydrogen production, because the increase of applied overpotential can result in a significant increase in current density. To the best of our knowledge, a Tafel slope of ~30 mV/decade is the state-of-the-art value achieved by electrocatalysts based on earth-abundant elements. The reason why p-$CoSe_2$ is more active than the single crystals (c-$CoSe_2$ and CoSe) and amorphous $CoSe_x$ might be that the mixed crystals (c-$CoSe_2$ and o-$CoSe_2$) give the benefit of chemisorbing of H atoms in the Tafel reaction. More works such as theoretical calculation are required to reveal the mechanism of HER on p-$CoSe_2$ at the molecular level.

Galvanostatic measurements at a constant current density of −10 mA/cm^2 were used to evaluate the stability of p-$CoSe_2$ (300 °C) under HER operating conditions. It was found that the cathodic overpotential required to maintain $J_{cathodic}$ = −10 mA/cm^2 increased by only about 8 mV after 40 h, as shown in Figure 5H, indicating an excellent stability of p-$CoSe_2$.

CONCLUSION

In this study, we present a cheap and efficient HER catalyst, i.e., polymorphic $CoSe_2$ with mixed orthorhombic and cubic phases by calcining $CoSe_x$ at 300 °C. The HER performance of polymorphic $CoSe_2$ is quite superior to that of amorphous $CoSe_x$, cubic $CoSe_2$, and CoSe. Polymorphic $CoSe_2$ exhibited a Tafel slope of ~30 mV/decade, which is the smallest Tafel slope reported for electrocatalysts based on earth-abundant elements. The superior HER activity of polymorphic $CoSe_2$ is possibly attributed to the enhanced chemisorbing of H atoms in the Tafel reaction. This work provides a new strategy for the future development of highly active HER catalysts based on earth-abundant elements.

ASSOCIATED CONTENT

Supporting Information

Detailed synthetic procedures, SEM, TEM, XPS, and corresponding electrochemistry data. This material is available free of charge via the Internet at http://pubs.acs.org.

AUTHOR INFORMATION

Corresponding Author

*E-mail: xwzhang@zju.edu.cn. Fax: +86-571-87952525.

Notes

The authors declare no competing financial interest.

ACKNOWLEDGMENTS

Financial support was received from the Natural Science Foundation of China (Project No. 21276231, 21476201, U1462201, and U1162128).

REFERENCES

(1) Lewis, N. S.; Nocera, D. G. Powering the Planet: Chemical Challenges in Solar Energy Utilization. *Proc. Natl. Acad. Sci. U. S. A.* **2006**, *103*, 15729−15735.

(2) Tachibana, Y.; Vayssieres, L.; Durrant, J. R. Artificial Photosynthesis for Solar Water-Splitting. *Nat. Photonics* **2012**, *6*, 511−518.

(3) Walter, M. G.; Warren, E. L.; McKone, J. R.; Boettcher, S. W.; Mi, Q.; Santori, E. A.; Lewis, N. S. Solar Water Splitting Cells. *Chem. Rev.* **2010**, *110*, 6446−6473.

(4) Faber, M. S.; Jin, S. Earth-Abundant Inorganic Electrocatalysts and Their Nanostructures for Energy Conversion Applications. *Energy Environ. Sci.* **2014**, *7*, 3519−3542.

(5) Jun, Y.-S.; Park, J.; Lee, S. U.; Thomas, A.; Hong, W. H.; Stucky, G. D. Three-Dimensional Macroscopic Assemblies of Low-Dimensional Carbon Nitrides for Enhanced Hydrogen Evolution. *Angew. Chem., Int. Ed.* **2013**, *125*, 11289−11293.

(6) Shalom, M.; Gimenez, S.; Schipper, F.; Herraiz-Cardona, I.; Bisquert, J.; Antonietti, M. Controlled Carbon Nitride Growth on Surfaces for Hydrogen Evolution Electrodes. *Angew. Chem., Int. Ed.* **2014**, *126*, 3728−3732.

(7) Chen, W.-F.; Sasaki, K.; Ma, C.; Frenkel, A. I.; Marinkovic, N.; Muckerman, J. T.; Zhu, Y.; Adzic, R. R. Hydrogen-Evolution Catalysts Based on Non-Noble Metal Nickel−Molybdenum Nitride Nanosheets. *Angew. Chem., Int. Ed.* **2012**, *51*, 6131−6135.

(8) Liu, Q.; Tian, J.; Cui, W.; Jiang, P.; Cheng, N.; Asiri, A. M.; Sun, X. Carbon Nanotubes Decorated with CoP Nanocrystals: A Highly Active Non-Noble-Metal Nanohybrid Electrocatalyst for Hydrogen Evolution. *Angew. Chem., Int. Ed.* **2014**, *53*, 6710−6714.

(9) Wan, C.; Regmi, Y. N.; Leonard, B. M. Multiple Phases of Molybdenum Carbide as Electrocatalysts for the Hydrogen Evolution Reaction. *Angew. Chem., Int. Ed.* **2014**, *53*, 6407−6410.

(10) Yan, Y.; Xia, B.; Xu, Z.; Wang, X. Recent Development of Molybdenum Sulfides as Advanced Electrocatalysts for Hydrogen Evolution Reaction. *ACS Catal.* **2014**, *4*, 1693−1705.

(11) Merki, D.; Hu, X. L. Recent Developments of Molybdenum and Tungsten Sulfides as Hydrogen Evolution Catalysts. *Energy Environ. Sci.* **2011**, *4*, 3878−3888.

(12) Nørskov, J. K.; Bligaard, T.; Logadottir, A.; Kitchin, J. R.; Chen, J. G.; Pandelov, S.; Stimming, U. Trends in the Exchange Current for Hydrogen Evolution. *J. Electrochem. Soc.* **2005**, *152*, J23−J26.

(13) Jaramillo, T. F.; Jørgensen, K. P.; Bonde, J.; Nielsen, J. H.; Horch, S.; Chorkendorff, I. Identification of Active Edge Sites for Electrochemical H_2 Evolution from MoS_2 Nanocatalysts. *Science* **2007**, *317*, 100−102.

DOI: 10.1021/am507373g
ACS Appl. Mater. Interfaces 2015, 7, 1772−1779

(14) Cheng, L.; Huang, W.; Gong, Q.; Liu, C.; Liu, Z.; Li, Y.; Dai, H. Ultrathin WS_2 Nanoflakes as a High-Performance Electrocatalyst for the Hydrogen Evolution Reaction. *Angew. Chem., Int. Ed.* **2014**, *53*, 7860−7863.
(15) Tang, H.; Dou, K. P.; Kaun, C. C.; Kuang, Q.; Yang, S. H. $MoSe_2$ Nanosheets and Their Graphene Hybrids: Synthesis, Characterization and Hydrogen Evolution Reaction Studies. *J. Mater. Chem. A* **2014**, *2*, 360−364.
(16) Faber, M. S.; Dziedzic, R.; Lukowski, M. A.; Kaiser, N. S.; Ding, Q.; Jin, S. High-Performance Electrocatalysis Using Metallic Cobalt Pyrite (CoS_2) Micro- and Nanostructures. *J. Am. Chem. Soc.* **2014**, *136*, 10053−10061.
(17) Zhang, H.; Lei, L.; Zhang, X. One-Step Synthesis of Cubic Pyrite-Type $CoSe_2$ at Low Temperature for Efficient Hydrogen Evolution Reaction. *RSC Adv.* **2014**, *4*, 54344−54348.
(18) Kong, D.; Wang, H.; Lu, Z.; Cui, Y. $CoSe_2$ Nanoparticles Grown on Carbon Fiber Paper: An Efficient and Stable Electrocatalyst for Hydrogen Evolution Reaction. *J. Am. Chem. Soc.* **2014**, *136*, 4897−4900.
(19) Kong, D.; Cha, J. J.; Wang, H.; Lee, H. R.; Cui, Y. First-Row Transition Metal Dichalcogenide Catalysts for Hydrogen Evolution Reaction. *Energy Environ. Sci.* **2013**, *6*, 3553−3558.
(20) Chen, W. F.; Wang, C. H.; Sasaki, K.; Marinkovic, N.; Xu, W.; Muckerman, J. T.; Zhu, Y.; Adzic, R. R. Highly Active and Durable Nanostructured Molybdenum Carbide Electrocatalysts for Hydrogen Production. *Energy Environ. Sci.* **2013**, *6*, 943−951.
(21) Yan, Y.; Xia, B. Y.; Qi, X. Y.; Wang, H. B.; Xu, R.; Wang, J. Y.; Zhang, H.; Wang, X. Nano-Tungsten Carbide Decorated Graphene as Co-Catalysts for Enhanced Hydrogen Evolution on Molybdenum Disulfide. *Chem. Commun.* **2013**, *49*, 4884−4886.
(22) Vrubel, H.; Hu, X. L. Molybdenum Boride and Carbide Catalyze Hydrogen Evolution in Both Acidic and Basic Solutions. *Angew. Chem., Int. Ed.* **2012**, *51*, 12703−12706.
(23) Chen, W.-F.; Muckerman, J. T.; Fujita, E. Recent Developments in Transition Metal Carbides and Nitrides as Hydrogen Evolution Electrocatalysts. *Chem. Commun.* **2013**, *49*, 8896−8909.
(24) Popczun, E. J.; McKone, J. R.; Read, C. G.; Biacchi, A. J.; Wiltrout, A. M.; Lewis, N. S.; Schaak, R. E. Nanostructured Nickel Phosphide as an Electrocatalyst for the Hydrogen Evolution Reaction. *J. Am. Chem. Soc.* **2013**, *135*, 9267−9270.
(25) Liu, Q.; Tian, J.; Cui, W.; Jiang, P.; Cheng, N.; Asiri, A. M.; Sun, X. Carbon Nanotubes Decorated with Cop Nanocrystals: A Highly Active Non-Noble-Metal Nanohybrid Electrocatalyst for Hydrogen Evolution. *Angew. Chem., Int. Ed.* **2014**, *53*, 6710−6714.
(26) Popczun, E. J.; Read, C. G.; Roske, C. W.; Lewis, N. S.; Schaak, R. E. Highly Active Electrocatalysis of the Hydrogen Evolution Reaction by Cobalt Phosphide Nanoparticles. *Angew. Chem., Int. Ed.* **2014**, *53*, 5427−5430.
(27) Xing, Z. C.; Liu, Q.; Asiri, A. M.; Sun, X. P. Closely Interconnected Network of Molybdenum Phosphide Nanoparticles: A Highly Efficient Electrocatalyst for Generating Hydrogen from Water. *Adv. Mater.* **2014**, *26*, 5702−5707.
(28) Liao, L.; Wang, S. N.; Xiao, J. J.; Bian, X. J.; Zhang, Y. H.; Scanlon, M. D.; Hu, X. L.; Tang, Y.; Liu, B. H.; Girault, H. H. A Nanoporous Molybdenum Carbide Nanowire as an Electrocatalyst for Hydrogen Evolution Reaction. *Energy Environ. Sci.* **2014**, *7*, 387−392.
(29) Yan, Y.; Xia, B. Y.; Ge, X. M.; Liu, Z. L.; Wang, J. Y.; Wang, X. Ultrathin MoS_2 Nanoplates with Rich Active Sites as Highly Efficient Catalyst for Hydrogen Evolution. *ACS Appl. Mater. Interfaces* **2013**, *5*, 12794−12798.
(30) Morales-Guio, C. G.; Stern, L. A.; Hu, X. Nanostructured Hydrotreating Catalysts for Electrochemical Hydrogen Evolution. *Chem. Soc. Rev.* **2014**, *43*, 6555−6569.
(31) Tian, J. Q.; Liu, Q.; Asiri, A. M.; Sun, X. P. Self-Supported Nanoporous Cobalt Phosphide Nanowire Arrays: An Efficient 3d Hydrogen-Evolving Cathode over the Wide Range of Ph 0−14. *J. Am. Chem. Soc.* **2014**, *136*, 7587−7590.
(32) Xie, J. F.; Zhang, H.; Li, S.; Wang, R. X.; Sun, X.; Zhou, M.; Zhou, J. F.; Lou, X. W.; Xie, Y. Defect-Rich MoS_2 Ultrathin Nanosheets with Additional Active Edge Sites for Enhanced Electrocatalytic Hydrogen Evolution. *Adv. Mater.* **2013**, *25*, 5807−5813.
(33) Gu, S.; Du, H.; Asiri, A. M.; Sun, X.; Li, C. M. Three-Dimensional Interconnected Network of Nanoporous CoP Nanowires as an Efficient Hydrogen Evolution Cathode. *Phys. Chem. Chem. Phys.* **2014**, *16*, 16909−16913.
(34) Chang, Y.-H.; Lin, C.-T.; Chen, T.-Y.; Hsu, C.-L.; Lee, Y.-H.; Zhang, W. J.; Wei, K.-H.; Li, L.-J. Highly Efficient Electrocatalytic Hydrogen Production by MoS_x Grown on Graphene-Protected 3d Ni Foams. *Adv. Mater.* **2013**, *25*, 756−760.
(35) Yang, J.; Voiry, D.; Ahn, S. J.; Kang, D.; Kim, A. Y.; Chhowalla, M.; Shin, H. S. Two-Dimensional Hybrid Nanosheets of Tungsten Disulfide and Reduced Graphene Oxide as Catalysts for Enhanced Hydrogen Evolution. *Angew. Chem., Int. Ed.* **2013**, *52*, 13751−13754.
(36) Lukowski, M. A.; Daniel, A. S.; Meng, F.; Forticaux, A.; Li, L. S.; Jin, S. Enhanced Hydrogen Evolution Catalysis from Chemically Exfoliated Metallic MoS_2 Nanosheets. *J. Am. Chem. Soc.* **2013**, *135*, 10274−10277.
(37) Voiry, D.; Yamaguchi, H.; Li, J.; Silva, R.; Alves, D. C. B.; Fujita, T.; Chen, M.; Asefa, T.; Shenoy, V. B.; Eda, G.; Chhowalla, M. Enhanced Catalytic Activity in Strained Chemically Exfoliated WS_2 Nanosheets for Hydrogen Evolution. *Nat. Mater.* **2013**, *12*, 850−855.
(38) Merki, D.; Fierro, S.; Vrubel, H.; Hu, X. L. Amorphous Molybdenum Sulfide Films as Catalysts for Electrochemical Hydrogen Production in Water. *Chem. Sci.* **2011**, *2*, 1262−1267.
(39) Faber, M. S.; Lukowski, M. A.; Ding, Q.; Kaiser, N. S.; Jin, S. Earth-Abundant Metal Pyrites (FeS_2, CoS_2, NiS_2, and Their Alloys) for Highly Efficient Hydrogen Evolution and Polysulfide Reduction Electrocatalysis. *J. Phys. Chem. C* **2014**, *118*, 21347−21356.
(40) Xie, J. F.; Zhang, J. J.; Li, S.; Grote, F.; Zhang, X. D.; Zhang, H.; Wang, R. X.; Lei, Y.; Pan, B. C.; Xie, Y. Controllable Disorder Engineering in Oxygen-Incorporated MoS_2 Ultrathin Nanosheets for Efficient Hydrogen Evolution. *J. Am. Chem. Soc.* **2013**, *135*, 17881−17888.
(41) Sun, Y.; Liu, C.; Grauer, D. C.; Yano, J.; Long, J. R.; Yang, P.; Chang, C. J. Electrodeposited Cobalt-Sulfide Catalyst for Electrochemical and Photoelectrochemical Hydrogen Generation from Water. *J. Am. Chem. Soc.* **2013**, *135*, 17699−17702.
(42) Carim, A. I.; Saadi, F. H.; Soriaga, M. P.; Lewis, N. S. Electrocatalysis of the Hydrogen-Evolution Reaction by Electrodeposited Amorphous Cobalt Selenide Films. *J. Mater. Chem. A* **2014**, *2*, 13835−13839.
(43) Velazquez, J. M.; Saadi, F. H.; Pieterick, A. P.; Spurgeon, J. M.; Soriaga, M. P.; Brunschwig, B. S.; Lewis, N. S. Synthesis and Hydrogen-Evolution Activity of Tungsten Selenide Thin Films Deposited on Tungsten Foils. *J. Electroanal. Chem.* **2014**, *716*, 45−48.
(44) Feng, Y.; He, T.; Alonso-Vante, N. Carbon-Supported $CoSe_2$ Nanoparticles for Oxygen Reduction Reaction in Acid Medium. *Fuel Cells* **2010**, *10*, 77−83.
(45) Yang, J.; Shen, X.; Ji, Z.; Zhu, G. Reduced Graphene Oxide/$CoSe_2$ Nanocomposites: Hydrothermal Synthesis and Their Enhanced Electrocatalytic Activity. *J. Mater. Sci.* **2013**, *48*, 7913−7919.
(46) Nekooi, P.; Akbari, M.; Amini, M. K. Cose Nanoparticles Prepared by the Microwave-Assisted Polyol Method as an Alcohol and Formic Acid Tolerant Oxygen Reduction Catalyst. *Int. J. Hydrogen Energy* **2010**, *35*, 6392−6398.
(47) Susac, D.; Sode, A.; Zhu, L.; Wong, P.; Teo, M.; Bizzotto, D.; Mitchell, K.; Parsons, R.; Campbell, S. A Methodology for Investigating New Nonprecious Metal Catalysts for Pem Fuel Cells. *J. Phys. Chem. B* **2006**, *110*, 10762−10770.
(48) Cao, B.; Veith, G. M.; Neuefeind, J. C.; Adzic, R. R.; Khalifah, P. G. Mixed Close-Packed Cobalt Molybdenum Nitrides as Non-Noble Metal Electrocatalysts for the Hydrogen Evolution Reaction. *J. Am. Chem. Soc.* **2013**, *135*, 19186−19192.
(49) van der Heide, H.; H, R.; van Bruggen, C. F.; Haas, C. X-Ray Photoelectron Spectra of 3d Transition Metal Pyrites. *J. Solid State Chem.* **1980**, *33*, 17−25.

DOI: 10.1021/am507373g
ACS Appl. Mater. Interfaces 2015, 7, 1772−1779

(50) Zhang, Z.; Pang, S.; Xu, H.; Yang, Z.; Zhang, X.; Liu, Z.; Wang, X.; Zhou, X.; Dong, S.; Chen, X.; Gu, L.; Cui, G. Electrodeposition of Nanostructured Cobalt Selenide Films Towards High Performance Counter Electrodes in Dye-Sensitized Solar Cells. *RSC Adv.* **2013**, *3*, 16528−16533.
(51) Li, H.; Gao, D.; Cheng, X. Simple Microwave Preparation of High Activity Se-Rich $CoSe_2$/C for Oxygen Reduction Reaction. *Electrochim. Acta* **2014**, *138*, 232−239.
(52) Mandale, A. B.; Badrinarayanan, S.; Date, S. K.; Sinha, A. P. B. Photoelectron-Spectroscopic Study of Nickel, Manganese and Cobalt Selenides. *J. Electron Spectrosc. Relat. Phenom.* **1984**, *33*, 61−72.
(53) Sun, R. S.; Chan, M. K. Y.; Ceder, G. First-Principles Electronic Structure and Relative Stability of Pyrite and Marcasite: Implications for Photovoltaic Performance. *Phys. Rev. B* **2011**, *83*, 235311−235311.
(54) Feng, Y. J.; He, T.; Alonso-Vante, N. Carbon-Supported $CoSe_2$ nanoparticles for Oxygen Reduction Reaction in Acid Medium. *Fuel Cells* **2009**, *10*, 77−83.
(55) Wang, J.; Fan, W.; Yang, J.; Da, Z.; Yang, X.; Chen, K.; Yu, H.; Cheng, X. Tetragonal-Orthorhombic-Cubic Phase Transitions in Ag_2Se Nanocrystals. *Chem. Mater.* **2014**, *26*, 5647−5653.
(56) Kingery, W. D.; Bowen, H. K.; Uhlmann, D. R. *Introduction to Ceramics*, 2nd ed.; Wiley: New York, 1991.
(57) Cabán-Acevedo, M.; Liang, D.; Chew, K. S.; DeGrave, J. P.; Kaiser, N. S.; Jin, S. Synthesis, Characterization, and Variable Range Hopping Transport of Pyrite (FeS_2) Nanorods, Nanobelts, and Nanoplates. *ACS Nano* **2013**, *7*, 1731−1739.
(58) Navarro-Flores, E.; Chong, Z.; Omanovic, S. Characterization of Ni, NiMo, NiW and NiFe Electroactive Coatings as Electrocatalysts for Hydrogen Evolution in an Acidic Medium. *J. Mol. Catal. A: Chem.* **2005**, *226*, 179−197.
(59) Damian, A.; Omanovic, S. Ni and Nimo Hydrogen Evolution Electrocatalysts Electrodeposited in a Polyaniline Matrix. *J. Power Sources* **2006**, *158*, 464−476.
(60) Azizi, O.; Jafarian, M.; Gobal, F.; Heli, H.; Mahjani, M. G. The Investigation of the Kinetics and Mechanism of Hydrogen Evolution Reaction on Tin. *Int. J. Hydrogen Energy* **2007**, *32*, 1755−1761.
(61) Savadogo, O.; Ndzebet, E. Influence of $Siw_{12}O_{40}^{4-}$ on the Electrocatalytic Behaviour of Pt−Co Alloy Supported on Carbon for Water Electrolysis in 3 M KOH Aqueous Solution. *Int. J. Hydrogen Energy* **2001**, *26*, 213−218.
(62) Li, Y.; Wang, H.; Xie, L.; Liang, Y.; Hong, G.; Dai, H. MoS_2 nanoparticles Grown on Graphene: An Advanced Catalyst for the Hydrogen Evolution Reaction. *J. Am. Chem. Soc.* **2011**, *133*, 7296−7299.

DOI: 10.1021/am507373g
ACS Appl. Mater. Interfaces 2015, 7, 1772−1779